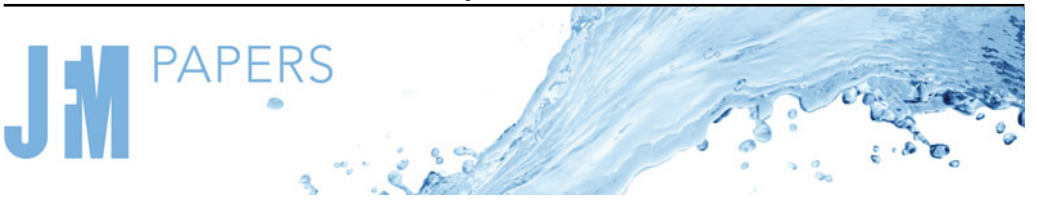
J. Fluid Mech. (2025), *vol.* 1022, A18, doi:10.1017/jfm.2025.10778



Free surface vortex dynamics during water-to-air amphibious rotor transitions

Logan Patrick Honts[1], **Yuanhang Zhu**[2] and **Daniel B. Quinn**[1,3]

[1]Department of Mechanical and Aerospace Engineering, University of Virginia, Charlottesville, VA 22904, USA

[2]Department of Mechanical Engineering, University of California, Riverside, CA 92521, USA

[3]Department of Electrical and Computer Engineering, University of Virginia, Charlottesville, VA 22904, USA

Corresponding author: Logan Patrick Honts, lph6cy@virginia.edu

(Received 19 June 2025; revised 11 September 2025; accepted 30 September 2025)

Amphibious unmanned vehicles promise next-generation water-based missions by eliminating the need for multiple vehicles to traverse water and air separately. Existing research-grade quadrotors can navigate in water and air and cross the water–air boundary, but it remains unclear how their transition is affected by rotor kinematics and geometry. We present here experimental results from isolated small rotors (diameters ~ 10 cm) dynamically transitioning from water to air. We discovered that rotors experience an abrupt change in frequency, lift and torque before reaching the interface, and the change is linked to the surface depression caused by a free surface vortex. We explored how the surface dynamics are affected by advance ratio, rotor diameter, number of rotor blades and input throttle. Free surface vortices above rotating objects have been studied in the context of unbaffled stirred tanks, but not in the field of small amphibious rotorcraft. We show that existing free surface vortex models can be adapted to explain water-to-air rotor performance. A better understanding of water–air rotor transitions helps to (i) assess the amphibious capability of existing aerial rotors, and (ii) suggest efficient water–air transition strategies for next-generation amphibious vehicles.

Key words: multiphase flow, vortex dynamics

1. Introduction

Amphibious unmanned aerial vehicles (AUAVs) are vehicles that can navigate in both water and air. Their multi-media versatility could enable new kinds of missions, such as

© The Author(s), 2025. Published by Cambridge University Press. This is an Open Access article, distributed under the terms of the Creative Commons Attribution licence (https://creativecommons.org/licenses/by/4.0/), which permits unrestricted re-use, distribution and reproduction, provided the original article is properly cited.

https://doi.org/10.1017/jfm.2025.10778 Published online by Cambridge University Press

long-distance water quality assessment or underwater mapping (Manoharan *et al.* 2021). For such a vehicle to be most useful, it should be able to transition between water and air smoothly and rapidly. Most existing vehicles are designed for air-only or water-only operation; for the few amphibious vehicles that exist, the water-to-air transition is plagued by roll/pitch/yaw instabilities (Suming & Weicheng 2019). For approximately a decade, roboticists have been experimenting with ways to more effectively transition from water to air.

Existing small-scale AUAVs (rotor diameters ~ 10 cm) use a range of techniques to cross the water–air interface. The Naviator I activates four pairs of coaxial rotors in sequence to avoid rotors operating directly at the interface (Maia, Soni & Diez 2015). The Mini UAUV uses a single set of rotors but changes its control scheme when an interface is detected (Zha *et al.* 2019). A prototype by Li *et al.* (2022) uses morphing rotors that automatically change shape based on the density of the surrounding media. Others have avoided dynamical transitions entirely by using controllable buoyancy. Both the Loon Copter (Alzu'bi *et al.* 2018) and the NEZHA (Lu *et al.* 2019) use positive buoyancy to breach the surface, then take off using rotors that are surrounded by air. Some of the challenges of transitioning were characterised by Zha *et al.* (2019), who noted a shift in rotor frequency brought on by air entrainment.

A key challenge of designing for a water-to-air transition is that little is known about the dynamics of near-interface rotors at this scale. Other vortex flows, however, have been well studied at this scale, such as those that appear in draining tanks (Andersen *et al.* 2003) or magnetically rotated flows (Vogt *et al.* 2013), and we propose that the most relevant existing literature concerns self-aerating unbaffled stirred tanks. In these tanks, submerged rotating blades create a free surface vortex, and if the vortex reaches the blades, air is entrained into a multiphase turbulent self-aerating flow. Building on the principles of Nagata (1975), studies have used analytical vortex models to link mixing behaviour with variables like blade diameter and frequency. For example, Halász *et al.* (2007) used a Burgers vortex to model magnetic stirring in a beaker, and Kim & Kim (2021) and Busciglio, Caputo & Scargiali (2013) used Rankine vortices to model the flow above a submerged rotating disk and a Rushton turbine. In stirred tanks, the impeller depth is fixed and the impeller and tank are comparably sized; it is unclear how a non-zero advance ratio (i.e. J, the ratio of forward flow velocity to rotational velocity of the rotor) and a large tank-to-rotor ratio will affect the interfacial vortex dynamics. These studies are also less concerned with forces on the rotors, whereas in the case of amphibious rotor dynamics, forces are a critical metric for performance.

To support the nascent field of amphibious rotorcraft hydrodynamics, we built a rig for testing an isolated rotor as it breaches a water–air interface. As in self-aerating stirred tanks, the rotor creates a free surface vortex as it approaches the interface from below. The free surface is depressed above the vortex core, causing the rotor to contact the surface before rising above the steady-state surface height. This contact point is linked with a rise in frequency, similar to the frequency changes observed by Zha *et al.* (2019). We found that rotor–surface contact is also linked to a sudden drop in rotor lift and torque, and we show that vortex models can be used to scale the depth at which these shifts occur. Our hope is that models of transitioning rotor dynamics will contribute to next-generation amphibious vehicles – ones that do not just overcome but also leverage the physics of water–air interfaces.

2. Methods and materials

To study the water-to-air transition, we suspended an isolated rotor in a tank partially filled with water (figure 1*a*,*b*). We considered six off-the-shelf rotors with diameters d ranging

https://doi.org/10.1017/jfm.2025.10778 Published online by Cambridge University Press

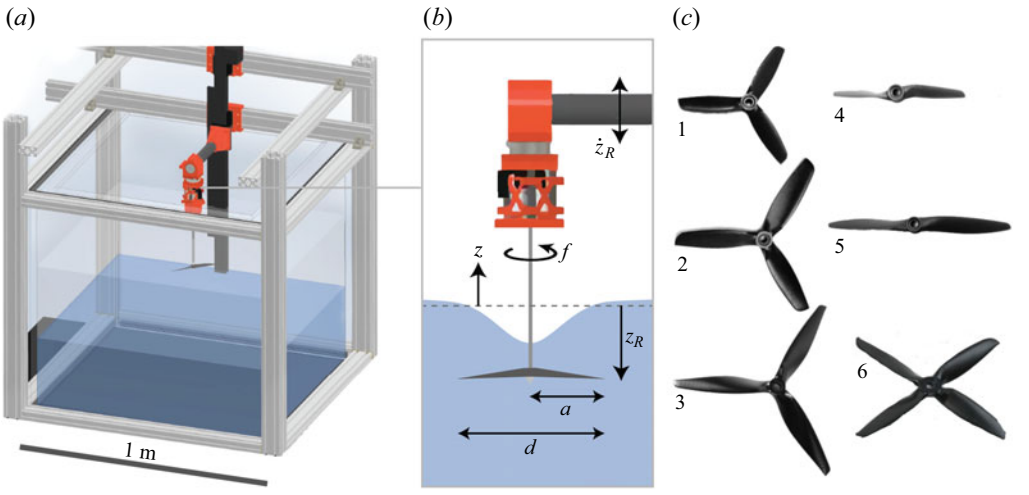


Figure 1. A schematic of the experimental set-up. (*a*) Glass testing tank; interior dimensions: 880 mm (width) × 910 mm (length) × 910 mm (height); wall thickness: 19 mm. (*b*) Rotor/motor assembly and traverse; rotor height z_R is defined relative to the no-flow steady-state surface, (*c*) six rotors tested; specifications in table 1.

from 100 to 150 mm (figure 1*c*). We chose rotors designed for air, because they tend to perform better in water than rotors designed for water do in air, and they have therefore been the preferred rotor type for AUAVs (Drews, Neto & Campos 2014). The rotors were centred in the tank, always more than two rotor diameters from the sidewalls and bottom, to minimise boundary effects (Deshpande *et al.* 2017 found that off-bottom clearances of this magnitude had no measurable effects on vortex height in a stirred tank). To limit the vast number of variables, we focused on rotors that were constant pitch, held parallel to the surface of the water and travelling vertically ($\pm z$) at a constant speed.

The rotors were spun by a stainless steel boat shaft (305 mm length, 4 mm diameter) driven by a brushless DC motor (DJI E800 350 kV). The motor was powered by a 24 V supply (Meanwell LRS-600-24), and its throttle T was controlled by a microcontroller via pulse width modulation (Arduino Mega 2560 + Castle Talon 35 ESC). The motor speed resulting from a given throttle was load-dependent and nonlinear, so we added a rotary encoder (US Digital E2) between the shaft and the motor to record the actual rotor frequency f. We tested five throttle settings: 10 %, 14 %, 16 %, 18 % and 20 %. Due to the high rotor loads underwater, throttles above 20 % were found to cause rotor breaks and motor burnout, so they were not considered.

The motor/rotor assembly was mounted to a vertical traverse to perform the water-to-air transition. The assembly was cantilevered away from the traverse via a carbon fibre tube (50 mm diameter) – a thick, round, lightweight cantilever was chosen to reduce vibrations. To measure the hydrodynamic forces and torques on the rotor, we mounted a six-axis transducer (ATI Mini40) between the motor and the carbon fibre tube. The tube was raised/lowered along a vertical guide rail by a stepper motor (Heechoo NEMA 23), and the actual vertical speed $\dot{z}_R$ was recorded using a linear encoder (US Digital EM2). We tested five vertical speeds: 20, 60, 100, 140, 180 mm s^{-1}, leading to advance ratios ($J = \dot{z}_R/(\mathrm{d}f)$) ranging from 0.01 to 0.17.

For each of the six rotors, the 25 combinations of throttle and ascent speed were tested in a random sequence. Each test began with the rotor two radii beneath the water–air interface ($z_R/a = -2$). After collecting 5 s of sensor calibration data, the rotor was commanded to spin, then – after a delay of 0.075 s to allow spinup – the traverse was commanded to move.

https://doi.org/10.1017/jfm.2025.10778 Published online by Cambridge University Press

		Rotor 1	Rotor 2	Rotor 3	Rotor 4	Rotor 5	Rotor 6
Radius a (mm)		51	64	76	52	76	64
# Blades		3	3	3	2	2	4
	r/a						
	0	–	–	–	–	–	–
	0.25	13.9	16.4	17.0	–	12.8	14.0
Local chord (mm)	0.5	14.8	17.3	16.7	10.4	13.6	14.8
	0.75	12.1	14.5	11.4	8.2	10.8	12.2
	1.00	0.2	0.3	0.2	0.3	0.1	0.2
	r/a						
	0	–	–	–	–	–	–
	0.25	55.6	67.5	95.1	–	65.9	75.8
Local pitch (mm)	0.5	85.6	94.0	104.4	104.1	101.5	92.6
	0.75	104.3	108.4	105.6	104.1	101.6	102.8
	1.00	109.2	114.3	106.7	104.1	88.3	106.7

Table 1. Rotor specifications. Rotors sourced from Advanced Precision Composites (APC) propellers, part numbers LP304040E-B4, LPB305040E-B4, LPBD306042E-B4, LP04141E, LP06041SF and LPBD405040E-B4. Rotors 1–5 have blades with even azimuthal spacing. Rotor 6 has two-axis symmetry and uneven azimuthal spacing. Locations along the span indicated with '–' are within the rotor's hub. Further rotor geometry details can be found in the Supplementary Materials, available at https://doi.org/10.1017/jfm.2025.10778.

The traverse raised the rotor assembly at a constant velocity $\dot{z}_R$ until $z_R/a = 4$. Once the rotor was at rest, an additional 5 s of calibration data were collected. Any sensor drift (typically ≈ 0.4 N / 2 h) was assumed to vary linearly with time and was subtracted from the raw data. Each test was repeated five times to give averages and standard deviations.

Sequencing, timing and post-processing were all handled by Matlab scripts. Encoder data were captured at 4000 Hz (then downsampled to 400 Hz) by a Data Acquisition Board (NI USB-6259), while force data were captured at 400 Hz by a wireless receiver. All data streams were passed through a low-pass filter (20 Hz cutoff for forces and torques; 10 Hz cutoff for the noisier frequency data). A comma-separated file listing all parameter combinations, trial numbers, timestamps, z-positions, rotor frequencies, forces and torques is available in the Supplementary Materials.

Note: we will focus our analysis on the frequency and lift (upwards force) of rotors as they rise upwards beneath a water–air interface ($-2 < z_R/a < 0$; $\dot{z}_R > 0$). This choice was motivated by (i) the similarity between trends in torque (τ) and lift (L) data, (ii) the unsurprising behaviours above water, i.e. ground effects in line with previous studies (Gao *et al.* 2019) and (iii) the unclear robotic relevance of amphibious rotors that operate while descending. We also repeated each trial with a longer spinup time of 1.075 s (vs. 0.075 s) to explore the effects of the initial condition. We will show that the initial condition had little effect on the transition region, and unless otherwise noted, we present trials with a 0.075 s spinup time. Nevertheless, we did capture frequency, lift and torque over the full z range in both directions ($-2 < z_R/a < 4$; $\pm\dot{z}_R$), and for both spinup times, and all raw data are available in the Supplementary Materials for interested readers.

3. Rotor and vortex dynamics

As a rotor approached the water–air interface from below, it experienced abrupt, yet predictable, changes in frequency, lift and torque. Consider, as a demonstration, the dynamics of rotor 2 at median conditions, $\dot{z}_R = 100\ \mathrm{mm\,s^{-1}}$ and 16 % throttle (figure 2). Far below the water, the rotor's frequency, lift and torque converged to equilibrium values,

https://doi.org/10.1017/jfm.2025.10778 Published online by Cambridge University Press

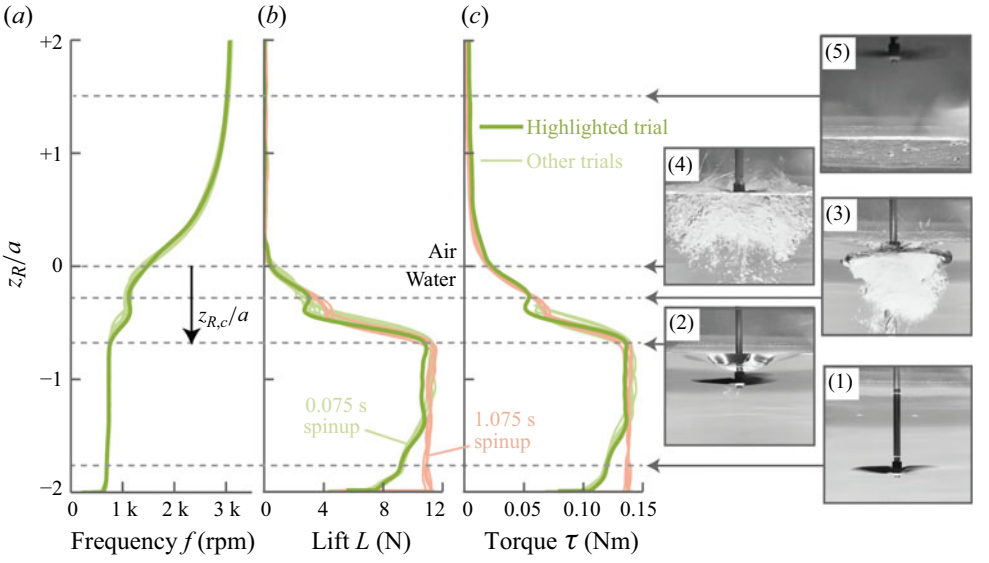


Figure 2. Representative vortex and rotor dynamics during water-to-air transition. Rotor 2; $\dot{z}_R = 100$ mm s^{-1}, throttle = 16 %. (*a*) Rotor frequency increases after $z_R > z_{R,c}$. (*b*) Rotor lift decreases after $z_R > z_{R,c}$. (*c*) Rotor torque follows lift trends. Insets: key moments of the highlighted trial (darker curve; Trial 1 in Movie 1): (1) far underwater, $z_R/a = -1.76$; (2) surface depression about to contact rotor, $z_R/a = -0.68$; (3) rotor–surface contact and subsequent aeration, $z_R/a = -0.28$; (4) breach, $z_R/a = 0$; (5) far above water, $z_R/a = +1.5$.

and the free surface became depressed, presumably due to the low-pressure core of the vortex produced by the rotor. In air, the rotor's frequency, lift and torque converged to different equilibrium values, as expected. However, at a critical transition depth $z_R = z_{R,c}$, well before the rotor passed the steady-state free surface, the frequency began to increase, while the lift and torque began to decrease. Video stills demonstrate that this early transition corresponds to the rotor reaching the depressed free surface ($z_R = \eta(0)$) before reaching the steady-state free surface ($z_R = 0$) (figure 2, insets). Across trials with the same input kinematics, the critical transition depth $z_{R,c}$ was largely unchanged.

Another notable feature of the vortex/rotor dynamics is the aeration caused by rotor–surface contact. Soon after the rotor reached the depressed surface, it often experienced a blip or inflection in frequency, lift and torque (figure 2). The inflection was more pronounced at lower ascent speeds. Consider, for example, a proxy for quantifying inflection during the transition: the tortuosity of the $L(z_R)$ data, i.e. the ratio of arc length to distance between end points for $z_{R,c} < z_R < 0$, $\int_{-z_{R,c}}^{0} \sqrt{1 + L'(z_R)^2}\mathrm{d}z_R \,/\, \sqrt{(L(z_{R,c}) - L(0))^2 + z_{R,c}^2}$. Averaged across all rotors, throttles and trials, the tortuosity was 1.272 ± 0.081 for $\dot{z}_R = 20$ mm s^{-1} and 1.003 ± 0.005 for $\dot{z}_R = 180$ mm s^{-1}. Video stills demonstrate that this inflection corresponded to the onset of aeration (figure 2, inset (3)). Beyond that point, but before the rotor exited the water, air was entrained into a bubble-rich turbulent wake beneath the rotor. This state is similar to the one induced purposefully in stirred tanks, where aeration enhances the mixing effects of a submerged impeller (Nagata 1975).

The spinup time had no noticeable effect on the transition depth. With the shorter spinup time (0.075 s), the frequency had time to converge before the rotor began its ascent, whereas the lift and torque did not (figure 2). For all cases, frequency, lift and torque converged to within 2 % of their steady-state values underwater in less than 1.075 s.

https://doi.org/10.1017/jfm.2025.10778 Published online by Cambridge University Press

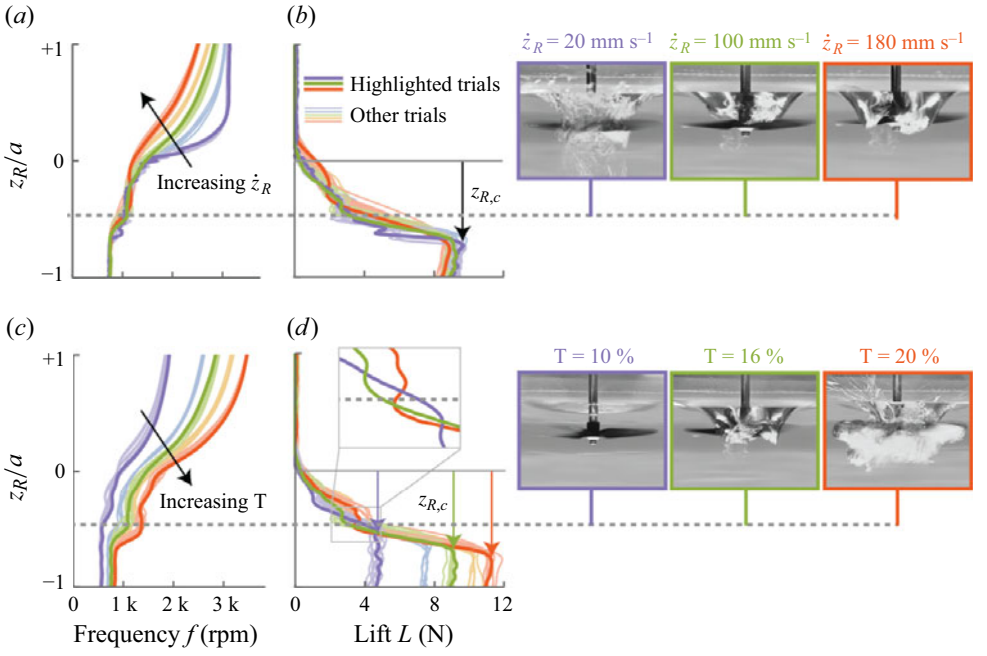


Figure 3. Vortex and rotor dynamics at differing ascent speeds and throttles. (*a*,*b*) Rotor frequency (*a*) and lift (*b*) begin transitioning at similar depths, $z_{R,c}$, regardless of ascent speed. (*c*,*d*) Rotor frequency (*c*) and lift (*d*) begin transitioning at lower depths as throttle increases. Insets: video snapshots at $z_R/a = -0.47$ in the highlighted trials (darker curves; Trial 2 in Movie 1).

Therefore, with the longer spinup time (1.075 s), frequency, lift and torque all converged before the ascent. The trials with longer spinup times are presumably more representative of water-to-air trajectories starting at deeper depths ($z_R/a < -2$), where secondary flows have time to evolve well before the transition. However, it seems that the initial conditions of these secondary flows have little effect on the transition depth.

The ascent speed $\dot{z}_R$ also appeared to have little effect on the critical depth at which the rotor contacted the free surface ($z_{R,c}$) (figure 3*a*,*b*). The depth of the surface depression therefore tended to be similar at a given rotor throttle and rotor depth across different ascent speeds (figure 3*a*,*b*, insets). This similarity is presumably what led to the similarity in frequency and lift curves beneath the water (above the water, the ascent speed $\dot{z}_R$ of the rotor led to different $f(z_R)$ curves; see figure 3*a*). The fact that ascent speed had little effect on the timing of rotor–surface contact suggests that the dynamics of the surface were largely quasi-steady. At higher advance ratios, unsteady effects would likely appear, but for the advance ratios considered here (0.01–0.17), ascent speed had no measurable effect on $z_{R,c}$.

In contrast, throttle did have an effect on the transition depth ($z_{R,c}$). As throttle increased, $z_{R,c}$ decreased, i.e. the stronger free vortex led to an earlier growth of the surface depression and subsequent contact with the rotor (figure 3*c*, *d*). Therefore, at a given rotor depth, the free surface was often in a qualitatively different stage depending on throttle. For example, when rotor 2 was at $z_R/a = -0.47$, the rotor was either below the free surface, just reaching the free surface or mid-aeration, depending on whether the throttle was 10 %, 16 % or 20 % (figure 3*c*, *d*, insets). This dependence on throttle is consistent with studies of stirred tanks, where higher impeller speeds lead to stronger free vortices and deeper surface depressions (Halász *et al.* 2007; Busciglio *et al.* 2013; Kim & Kim 2021). In the

https://doi.org/10.1017/jfm.2025.10778 Published online by Cambridge University Press

case of transitioning rotors, this dependence means that higher throttles cause frequency to rise and lift to drop at lower depths.

All six rotors that we tested had similar frequency, lift and torque trends as those of rotor 2 (figures 2 and 3). The only clear difference was that the transition depth ($z_{R,c}$) was lower when more blades were present. An effect of blade number is perhaps expected given that blade geometry also influences the effectiveness of impellers in stirred tanks (Pincovschi, Dragomirescu & Modrogan 2025). Rather than replotting frequency and lift curves, we will consider the effect of blade number/geometry when examining the scaling of $z_{R,c}$ in the following section.

4. Scaling the transition depth

Motivated by the links between the free vortex and the rotor's performance, we explored how transition depth ($z_{R,c}$) might scale with rotor geometry and kinematics. For a given rotor type, we propose that $z_{R,c}$ must be a function of the variables present: the acceleration due to gravity g, the rotor radius a, the rotor frequency f, the rotor ascent speed $\dot{z}_R$ and the density ρ, viscosity μ and surface tension γ of the surrounding water. Dimensional analysis reveals that the scaled transition depth must be some function ϕ of four dimensionless groups, e.g.

$$\frac{z_{R,c}}{a} = \phi\left(\frac{\dot{z}_R}{2af}, \frac{\rho g a^2}{\gamma}, \frac{\rho f a^2}{\mu}, \frac{fa}{\sqrt{ga}}\right) \equiv \phi(J,\, Bo,\, Re,\, Fr). \tag{4.1}$$

The first dimensionless group in ϕ is the advance ratio J. The other three are various ratios of gravity forces, surface tension forces, viscous forces and rotor-imposed inertial forces, i.e. they are forms of a Bond number Bo, Reynolds number Re and Froude number Fr.

Our results suggest no dependence on the advance ratio over the range considered here (figure 3*a*,*b*). The Bond number, a ratio of gravity to surface tension forces, was high throughout our study ($\approx$ 100 to 2700), and the rounded shape of the free surface – which differs from the needle-like profiles of vortices dominated by surface tension (Andersen *et al.* 2003) – suggests that Bo is not a key parameter here. The Reynolds number was also high throughout our study ($\approx$ 28 000 to 84 000), and studies of stirred tanks have found inviscid vortex models to work well for $Re \gtrapprox 10^4$ (Nagata 1975; Deshpande *et al.* 2017). In contrast, the Froude number based on rotor diameter, Fr, was $O(1)$ throughout our study ($\approx$ 0.7–1.5). In stirred tank literature, the Froude number based on impeller diameter has been described as the 'key dimensionless parameter for describing the vortex depth' (Deshpande *et al.* 2017). As we will show, the same conclusion can be drawn from our data.

Plotting transition depth against Froude number (figure 4) supports the hypothesis that $z_{R,c}/a$ is primarily a function of Fr. Not only does Froude number do well to collapse the transition depths for different rotor radii, but also the relationship is largely linear within each blade type. To test the linear scaling's robustness, we also produced nonlinear fits $z_{R,c}/a = \alpha Fr^{\beta}$ for the 2-, 3-,and 4-blade rotor data, with fit coefficients α and β. The fitted β values were near unity (0.93, 0.84 and 0.89) with residuals comparable to the purely linear fit ($R^2 = 0.78$, 0.82, 0.92), supporting the claim that $z_{R,c}/a \propto -Fr$.

5. Vortex modelling

We wondered if the observed scaling of $z_{R,c}$ could be better understood using a Burgers vortex, a steady solution to the Navier–Stokes equations in which an inward radial flow and an outward diffusion of vorticity balance to form a stable vortex (Drazin & Riley

https://doi.org/10.1017/jfm.2025.10778 Published online by Cambridge University Press

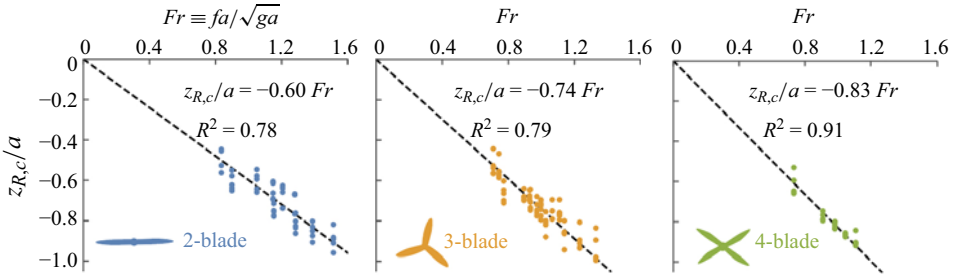


Figure 4. Scaled transition depth versus Froude number. The depth at which lift begins to drop ($z_{R,c}$), as calculated using derivative thresholding on $L(z_R)$ data, generally scales with Froude number for the 2-, 3- and 4-blade rotors.

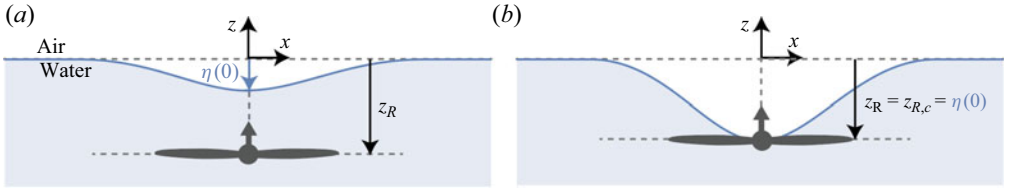


Figure 5. Model set-up. (*a*) As z_R rises, the surface depression grows. (*b*) As z_R rises to the transition depth, the rotor contacts the free surface ($z_R = z_{R,c} = \eta(0)$).

2006). The Burgers vortex has been successfully used to model a variety of vortex-related phenomena, including the free vortex in stirred tanks (Nagata 1975; Lugt 1983; Halász *et al.* 2007). In a Burgers vortex, a Gaussian distribution of vorticity centred at the origin leads to an azimuthal flow speed

$$u_\theta = \frac{\Gamma}{2\pi r}\left(1 - \mathrm{e}^{-\frac{r^2}{c^2}}\right), \tag{5.1}$$

where Γ is circulation and c is the vortex core radius. Far outside the core, the vortex converges to irrotational flow ($\lim_{r\to\infty} u_\theta = \Gamma/(2\pi r)$); deep in the core, the vortex converges to a solid body rotation ($\lim_{r\to 0} u_\theta = \Gamma r/(2\pi c^2)$).

Equation (5.1) can be used to model the depression of a free surface above the vortex. Following others (e.g. Halász *et al.* 2007), we equate the radial and vertical pressure gradients with the centrifugal force and gravity,

$$\frac{\partial p}{\partial r} = \frac{\rho u_\theta^2}{r} \quad \text{and} \quad \frac{\partial p}{\partial z} = -\rho g, \tag{5.2}$$

leading to a differential equation for the free surface height $\eta(r)$

$$\frac{\partial \eta}{\partial r} = -\frac{\partial p/\partial r}{\partial p/\partial z} = \frac{u_\theta^2}{rg}. \tag{5.3}$$

The height at the centre of the vortex (with $\eta(\infty) \equiv 0$; figure 5) follows from integration

$$\eta(0) = \int_\infty^0 \frac{u_\theta^2}{rg} = -\frac{\ln 2}{4\pi^2}\frac{\Gamma^2}{c^2 g}. \tag{5.4}$$

We expect the vortex core radius to scale with rotor radius ($c \sim a$) (Halász *et al.* 2007, see also free surface profiles in the Supplementary Materials). We expect the circulation

https://doi.org/10.1017/jfm.2025.10778 Published online by Cambridge University Press

to be primarily set by the rotor radius and tip speed (e.g. $\Gamma \sim fa^2$, Abedi 2011); however, studies of stirred tanks have found that vortex depth also includes a dependence on impeller height. For example, Halász *et al.* (2007) found that vortex strength Γ included a $1/\sqrt{z_R/a}$ dependence. What differs in our system is that the rotor rises and thus the vortex ultimately reaches the rotor in every case (figure 5*b*). We therefore expect $\eta(0) \sim z_{R,c}$ throughout much of the water-to-air transition phase. With $\eta(0) \sim z_{R,c}$, $c \sim a$ and $\Gamma \sim fa^2 \cdot (1/\sqrt{z_{R,c}/a})$ in (5.4) leads to

$$\frac{\eta(0)}{a} \sim -\frac{fa}{\sqrt{ga}} = -Fr. \tag{5.5}$$

The prediction that scaled vortex height would scale with Fr during the transition phase offers some physical rationale for the linear relation between transition depth and Froude number (figure 4). Curiously, in stirred tank studies, vortex depth is often found to scale with f^2, with additional geometric factors such as impeller depth also playing a role (Nagata 1975; Smit & During 1991; Halász *et al.* 2007; Busciglio *et al.* 2013; Deshpande *et al.* 2017). In our case, because the vortex depth and the rotor/impeller depth are inherently linked, it appears that the transition depth ultimately scales with f (5.5, figure 4).

6. Conclusion

Regardless of why $z_{R,c}$ scales with Fr, the fact that it does offers actionable guidelines for designing water-to-air transitioning rotors. If the dimensionless rotor depth (z_R/a) is scaled by Fr and plotted against the frequency and lift scaled by their equilibrium values underwater (f_0 and L_0), the resulting curves mostly collapse at the moment of rotor–surface contact (figure 6). Before the transition, the curves have different trajectories depending on the throttle and ascent speed, but they transition (experience the sharp rise in frequency and drop in lift) around the same point. The exceptions are the highest advance ratio cases, which do not have enough time to reach steady-state underwater conditions before reaching the transition depth. This discrepancy disappears when considering the longer spinup time data (1.075 s), where lift values have time to stabilise pre-transition (Supplementary Materials).

We chose to focus on cases with the shorter spinup time (0.075 s), because too long a spinup time leads to tank-dependent flows that are less relevant to amphibious rotorcraft. In stirred tank studies, spinup times can be minutes long, and the impeller can be less than two radii from the tank walls and close to or even touching the tank floor (Halász *et al.* 2007; Busciglio *et al.* 2013). These conditions produce tank-scale cores of recirculating flow perpendicular to the axis of spin, similar to Ekman pumping (Grants *et al.* 2008). To mitigate these effects, we ensured that each rotor in our study was >4 radii from the tank bottom and >4.75 radii from the tank walls at all times. Even so, very long spinup times (> 15 s) produced tank-scale recirculation in our set-up, hence our focus on shorter spinup times. We propose that these shorter spinup times ($O(0.1-1)$ s) are more representative of conditions around AUAV rotors, and under these conditions, the transition depth scales predictably with Froude number.

With a transition point governed by Froude number, one can predict how design variables will affect the depth at which a rotor experiences the sudden shifts in frequency and lift. With increasing rotor radius, it appears that $z_{R,c}$ increases with $a^{3/2}$ (or that $z_{R,c}/a$ increases with $a^{1/2}$). It also appears that $z_{R,c}$ increases with number of blades (figure 6*a*, *b*, *c*). These increases make physical sense because more blades and larger

https://doi.org/10.1017/jfm.2025.10778 Published online by Cambridge University Press

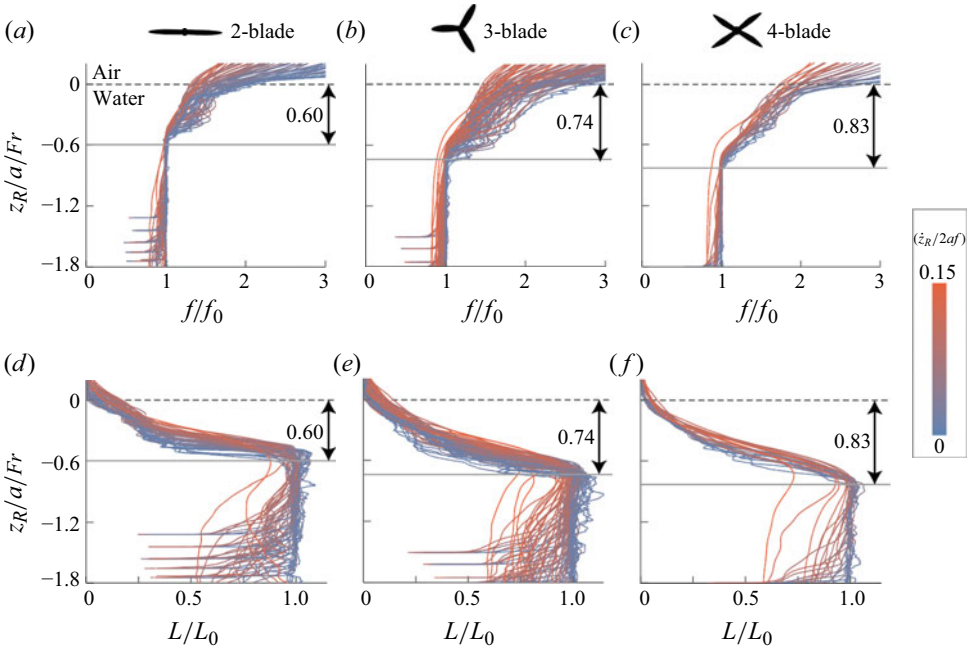


Figure 6. Frequency and lift scaling. When plotted against frequency and lift normalised by their equilibrium underwater values, the sudden shifts in frequency and lift occur at a consistent value of scaled rotor height that depends only on the number of blades when plotted against frequency (*a–c*) and lift (*d–f*).

rotors induce stronger flow rotation, which is the primary cause of the free surface depression (Yamamoto, Fang & Komarov 2019). Finally, it appears that $z_{R,c}$ increases linearly with frequency, differing from the frequency squared dependence in prior models from stirred tank studies (Halász *et al.* 2007). This difference may be due to the differing roles of recirculation caused by long spinup times and small rotor–tank separations. These predictions offer starting points for positioning coaxial rotor pairs (Maia *et al.* 2015), designing morphing rotor blades (Li *et al.* 2022) or developing other strategies towards a smoother and faster transition.

In summary, we found that rotors at AUAV scales (diameters $\sim$ 10 cm) experience rapid and uneven shifts in frequency, lift and torque as they approach a water–air interface from underneath. Our results reproduce on an isolated rotor the entrainment-driven frequency shifts that have been observed on real AUAVs during transition (Zha *et al.* 2019). We found that these shifts are linked to the rotor contacting the depressed surface and the subsequent aeration phase. Dimensionless analysis, a Burgers vortex framework and direct lift measurements suggest that the shifts are governed primarily by a Froude number, $fa/\sqrt{ga}$, consistent with prior stirred tank literature. These shifts were present whether the spinup time was 0.075 or 1.075 s – the former more representative of an AUAV in a transient flow near the surface, and the latter more representative of an AUAV ascending steadily from lower depths. Further studies could expand the model to explore the effects of variable ascent speeds or number of blades. Existing AUAVs focus on entering and exiting the water as fast as possible, or saving energy and avoiding it altogether (Suming & Weicheng 2019). Our hope is that better models of transitioning rotors can support strategies for amphibious capability that are more seamless, efficient and robust.

Supplementary material. Supplementary material is available at https://doi.org/10.1017/jfm.2025.10778.

https://doi.org/10.1017/jfm.2025.10778 Published online by Cambridge University Press

Acknowledgements. The authors would like to thank Q. Zhong and D. Carter for early project ideation, T. Han for assisting in model theorisation and our anonymous reviewers for the inspiration to test the robustness of our results under longer spinup times.

Funding. This work was made possible by funding from the University of Virginia and the National Science Foundation (grant number 2040351; Program Manager: R. Joslin).

Declaration of interests. The authors report no conflict of interest.

Data availability statement. The data that support the findings of this study are openly available in the University of Virginia Dataverse at https://doi.org/10.18130/V3/DWXYFJ. See JFM's research transparency policy for more information.

References

ABEDI, H. 2011 Aerodynamic loads on rotor blades. Master's thesis. Chalmers, Sweden.

ALZU'BI, H., MANSOUR, I. & RAWASHDEH, O. 2018 Loon Copter: implementation of a hybrid unmanned aquatic–aerial quadcopter with active buoyancy control. *J. Field Robot.* **35** (5), 764–778.

ANDERSEN, A., BOHR, T., STENUM, B., RASMUSSEN, J.J. & LAUTRUP, B. 2003 Anatomy of a bathtub vortex. *Phys. Rev. Lett.* **91** (10), 104502.

BUSCIGLIO, A., CAPUTO, G. & SCARGIALI, F. 2013 Free-surface shape in unbaffled stirred vessels: experimental study via digital image analysis. *Chem. Engng Sci.* **104**, 868–880.

DESHPANDE, S.S., KAR, K.K., WALKER, J., PRESSLER, J. & SU, W. 2017 An experimental and computational investigation of vortex formation in an unbaffled stirred tank. *Chem. Engng Sci.* **168**, 495–506.

DRAZIN, P.G. & RILEY, N. 2006 *The Navier–Stokes Equations: A Classification of Flows and Exact Solutions*. Cambridge University Press.

DREWS, P.L.J., NETO, A.A. & CAMPOS, M.F.M. 2014 Hybrid unmanned aerial underwater vehicle: modeling and simulation. In *2014 IEEE/RSJ International Conference on Intelligent Robots and Systems*, pp. 4637–4642. IEEE.

GAO, S., DI FRANCO, C., CARTER, D., QUINN, D. & BEZZO, N. 2019 Exploiting ground and ceiling effects on autonomous uav motion planning. In *2019 International Conference on Unmanned Aircraft Systems (ICUAS)*, pp. 768–777. IEEE.

GRANTS, I., ZHANG, C., ECKERT, S. & GERBETH, G. 2008 Experimental observation of swirl accumulation in a magnetically driven flow. *J. Fluid Mech.* **616**, 135–152.

HALÁSZ, G., GYÜRE, B., JÁNOSI, I.M., SZABÓ, K.G. & TÉL, T. 2007 Vortex flow generated by a magnetic stirrer. *Am. J. Phys.* **75** (12), 1092–1098.

KIM, D. & KIM, D. 2021 Free-surface vortex formation and aeration by a submerged rotating disk. *Chem. Engng Sci.* **243**, 116787.

LI, L. *et al.* 2022 Aerial-aquatic robots capable of crossing the air-water boundary and hitchhiking on surfaces. *Sci. Robot.* vol. 7 (66), eabm6695.

LU, D., XIONG, C., ZENG, Z. & LIAN, L. 2019 A multimodal aerial underwater vehicle with extended endurance and capabilities. In *2019 International Conference on Robotics and Automation (ICRA)*, pp. 4674–4680. IEEE (Institute of Electrical and Electronics Engineers).

LUGT, H.J. 1983 *Vortex Flow in Nature and Technology*. Wiley.

MAIA, M.M., SONI, P. & DIEZ, F.J. 2015 Demonstration of an aerial and submersible vehicle capable of flight and underwater navigation with seamless air-water transition, arXiv: 1507.01932.

MANOHARAN, D., GAJENDRAN, C., PADMANABHAN, M.K., VIGNESH, S., RAJESH, S. & BHUVANESHWARAN, G.D. 2021 Design and development of autonomous amphibious unmanned aerial vehicle for in situ water quality assessment and water sampling. *J. Unmanned Vehicle Syst.* **9** (1), 182–204.

NAGATA, S. 1975 *Mixing: Principles and Applications. A Halsled Press book*. Kodansha.

PINCOVSCHI, I., DRAGOMIRESCU, A. & MODROGAN, C. 2025 Influence of impeller design on oxygen transfer in a stirred water tank with square cross-section. *Biochem. Engng J.* **216**, 109649.

SMIT, L. & DURING, J. 1991 Vortex geometry in stirred vessel. In *The Seventh European Congress of Mixing*, pp. 633–639. Royal Flemish Association of Engineers.

SUMING, Q. & WEICHENG, C. 2019 An overview on aquatic unmanned aerial vehicles. *Annu. Rev. Res.* **5** (3), 555663.

VOGT, T., GRANTS, I., ECKERT, S. & GERBETH, G. 2013 Spin-up of a magnetically driven tornado-like vortex. *J. Fluid Mech.* **736**, 641–662.

https://doi.org/10.1017/jfm.2025.10778 Published online by Cambridge University Press

YAMAMOTO, T., FANG, Y. & KOMAROV, S.V. 2019 Surface vortex formation and free surface deformation in an unbaffled vessel stirred by on-axis and eccentric impellers. *Chem. Engng J.* **367**, 25–36.

ZHA, J., THACHER, E., KROEGER, J., MÄKIHARJU, S.A. & MUELLER, M.W. 2019 Towards breaching a still water surface with a miniature unmanned aerial underwater vehicle. In *2019 International Conference on Unmanned Aircraft Systems (ICUAS)*, pp. 1178–1185. IEEE (Institute of Electrical and Electronics Engineers).

https://doi.org/10.1017/jfm.2025.10778 Published online by Cambridge University Press